

# Eulerian and Lagrangian velocity statistics in weakly forced two-dimensional turbulence

Michael K. Rivera and Robert E. Ecke

*The Condensed Matter and Thermal Physics Group (MPA-10) and The Center for NonLinear Studies (T-CNLS),  
Los Alamos National Laboratory, Los Alamos, NM, 87545*

(Dated: February 5, 2008)

We present statistics of velocity fluctuations in both the Lagrangian and Eulerian frame for weakly driven two-dimensional turbulence. We find that simultaneous inverse energy and enstrophy ranges present in the Lagrangian and Eulerian Fourier spectra are not directly echoed in real-space moments of velocity difference. The spectral ranges, however, do line up very well with ratios of the real-space moments *local* exponents, indicating that though the real-space moments are not scaling “nicely”, the relative behavior of the velocity difference probability distribution functions is changing over very short ranges of length scales. Utilizing this technique we show that the ratios of the local exponents for Eulerian moments in weak two-dimensional turbulence behave in agreement with Kolmogorov predictions over the spectrally identified ranges. The Lagrangian local exponent ratios, however, behave in a different manner compared to their Eulerian counterparts, and deviate significantly from what would be expected from Kolmogorov predictions.

PACS numbers: abc.123

## INTRODUCTION

There are two reference frames that are normally considered in turbulent fluids: the Eulerian frame and the Lagrangian frame [1, 2]. The Eulerian frame of motion is fixed to the laboratory frame where velocities, pressures and accelerations are fields fixed in space and varying with time (*i.e.*, the velocity field  $\mathbf{u}(\mathbf{x}, t)$ ). This frame has been used for many classical approaches to the turbulence problem, including the derivation of the Karman-Howarth equation and Kolmogorov scaling theory. The Lagrangian frame is fixed to fluid elements as they are advected by the turbulence. The position of the Lagrangian fluid element in time is denoted  $\mathbf{x}(t)$ , and the velocity and acceleration of the element are the first and second time derivative of the Lagrangian trajectory, respectively. The Lagrangian velocity at any time for any trajectory must equal its Eulerian counterpart (*i.e.*,  $\mathbf{u}(t) = \mathbf{u}(\mathbf{x}(t), t)$ ). The Lagrangian frame is a useful one when considering the mixing of scalars [3, 4, 5], such as a dye, by turbulent motion. The difficulties in making experimental measurement of Lagrangian trajectories has made the characterization of Lagrangian turbulence much less common, with a few results reported for two-dimensional turbulence [6, 7] and for three-dimensional turbulent flows [8, 9].

In either the Eulerian or Lagrangian frame, we would like to characterize the turbulent state by studying the statistical nature of the velocity fields by measuring, for example, spectra and moments of velocity differences. We define the Eulerian  $n^{\text{th}}$ -order moment of longitudinal velocity difference as

$$S^{(n)}(r) \equiv \langle ((\mathbf{u}(\mathbf{x} + \mathbf{r}) - \mathbf{u}(\mathbf{x})) \cdot \mathbf{r})^n \rangle, \quad (1)$$

and the Lagrangian  $n^{\text{th}}$  order moment of velocity differ-

ence as

$$D^{(n)}(\tau) \equiv \langle |\mathbf{u}(t + \tau) - \mathbf{u}(t)|^n \rangle. \quad (2)$$

We would like to extract ranges of spatial scales  $r$  for the Eulerian frame and time scales  $\tau$  for the Lagrangian frame over which the velocity statistics exhibit scaling and measure the corresponding scaling exponents. These exponents are then compared with theoretical prediction, when such predictions exist.

The moment characterization of the velocity fluctuations of turbulence is a standard procedure in fluid turbulence. Here we follow Frisch [2] with respect to this standard analysis paradigm. Velocity fluctuation moments have been experimentally obtained in three-dimensions for both the Eulerian and Lagrangian frames [9, 10]. Kolmogorov proved that for three-dimensional homogeneous isotropic turbulence,  $S^{(3)}(r) = -4/5\epsilon r$ , where  $\epsilon$  is the energy dissipation rate. Using dimensional analysis and the hypothesis of strict self-similarity, one can then show that  $S^{(n)}(r) \propto (\epsilon r)^{n/3}$ . Subsequent measurements of fluctuations in three-dimensional turbulent fluids demonstrate that strict self-similarity does not hold in these systems, and that there are significant deviations from the expected  $n/3$  scaling exponent, especially as  $r$  approaches the viscous dissipation scale and  $n$  becomes large [2]. This deviation is attributed to “intermittency”, a behavior in the spatial fluctuations of the velocity fields, characterized by bursts of activity. Intermittency is most commonly attributed to spatial fluctuations in the energy dissipation rate,  $\epsilon$  (note that  $\epsilon$  was assumed constant above) [2]. Accounting for this intermittency and the resultant adjustments to the Kolmogorov theory is still an active area of research.

Intermittency is also a feature of velocity statistics in the Lagrangian frame of three-dimensional turbulence. Recent experimental [9] and numerical [11] measurements

of Lagrangian velocity difference statistics demonstrate stronger deviations from similarity than were displayed in the Eulerian statistics. Though there is no exact result for  $D^{(n)}$  as there is for  $S^{(n)}$ , a dimensional argument suggests that  $D^{(n)}(\tau) \propto (\epsilon\tau)^{n/2}$  in the inertial energy range of scales. A more intermittent Lagrangian signal is perhaps not surprising; Kraichnan demonstrated [12] that even a non-intermittent Eulerian velocity field (albeit an unphysical one) could produce intermittent Lagrangian statistics.

As in three-dimensional turbulence, there are exact relations and similarity results for Eulerian statistics in two-dimensional turbulence [13, 14, 15, 16]. These results apply to both the inertial energy range of two-dimensional turbulence and the inertial enstrophy range. Unlike three-dimensional turbulence, the Eulerian signal of the inertial energy range of two-dimensional turbulence is non-intermittent and self-similar, yielding scaling exponents for  $S^{(n)}(r)$  in agreement with the expected  $r^{n/3}$  [13, 14]. Similarly, scaling exponents of  $S^{(n)}(r)$  for the Eulerian enstrophy range have the expected  $r^n$  behavior of the smooth velocity field at those scales. Although the scaling exponents in the enstrophy range are self-similar, the velocity difference moment may not be an adequate measurement tool to determine self-similarity for such smooth fields. This observation has resulted in the investigation of “inverse statistics” [17]. Analysis of our data using the inverse-statistics approach will be presented elsewhere.

Whereas Eulerian results have been measured previously for 2D turbulence [13, 15], corresponding results for Lagrangian velocity statistics have not been reported, perhaps owing to the difficulty in producing a two-dimensional system with significantly large scaling ranges for both energy and enstrophy. In three-dimensions, there is only a single inertial range in which the energy cascade range lies between the outer scale and the viscous scale. In two-dimensions there are two such ranges: an inverse-energy range analogous to the three dimensional energy range, and the direct enstrophy range. One therefore needs inertial behavior and measurements over a larger range of scales in two-dimensional systems than is needed in three. Unfortunately, it is typical for two-dimensional systems to have small ranges, which results in ambiguous scaling and a lack of self-consistency in how the ranges are defined.

When the ranges in question are small and the moments do not show unambiguous scaling behavior, no strong conclusions about scaling exponents can be made. Weaker conclusions can be drawn, however, using techniques such as extended self-similarity (ESS) [18], which explores the shape of the probability distribution functions (PDFs) within a range of scales. If the PDFs exhibit a range over which their shape is either constant, or has a particular trend, it is possible to extrapolate to the case where one had a more extended range with a given

scaling behavior.

In this paper we report measurements of velocity difference statistics in both the Eulerian and Lagrangian frames of two-dimensional turbulence. Moreover, we report these results for simultaneous energy and enstrophy ranges in our current system that is not significantly different from prior experiments. Owing to the limited extent of the ranges, we do not attempt to directly extract exponents of moments. Instead, we present ESS analysis of the *local* scaling exponents and demonstrate that the shape of the difference PDF’s evolves very differently in the Eulerian and Lagrangian frames. If this shape evolution applies for larger ranges, we can conclude that the velocity difference statistics in the Eulerian frame for both the energy and enstrophy scaling ranges are self-similar, whereas in the Lagrangian frame they are not.

## EXPERIMENTAL

Two-dimensional turbulence possessing simultaneous inverse energy and direct enstrophy cascades must be continuously forced [19]. One method for such forcing, originally pioneered by Dolzhansky in 1979 [20], is to subject a current carrying fluid to external magnetic fields. This method of forcing has since evolved into the stratified electromagnetic layer [21] which has become a common systems for the study of 2D turbulence.

The stratified electromagnetic layer consists of a dense salt water layer, typically 0.3 cm deep and 20 cm  $\times$  20 cm square, underneath a less dense solution of roughly the same depth. A current is passed in the plane of the layer, and the layers are subject to a spatially varying magnetic field penetrating them vertically. The resultant Lorentz force drives fluid motion. The evolution of the stratified layer system is expected to approximate the forced/damped 2D Navier-Stokes equation,

$$\frac{\partial u_i}{\partial t} + u_s \frac{\partial u_i}{\partial x_s} = -\frac{\partial p}{\partial x_i} + \nu \frac{\partial^2 u_i}{\partial x_i^2} - \alpha u_i + F_i, \quad (3)$$

supplemented by the incompressibility condition  $\partial_i u_i = 0$ , where  $\mathbf{u}$  is the fluid velocity field,  $p$  is the density normalized pressure,  $\mathbf{F}$  is the external electromagnetic

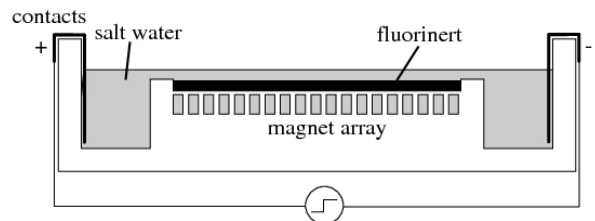


FIG. 1: Schematic illustration of the stratified-layer 2D turbulence experiment.

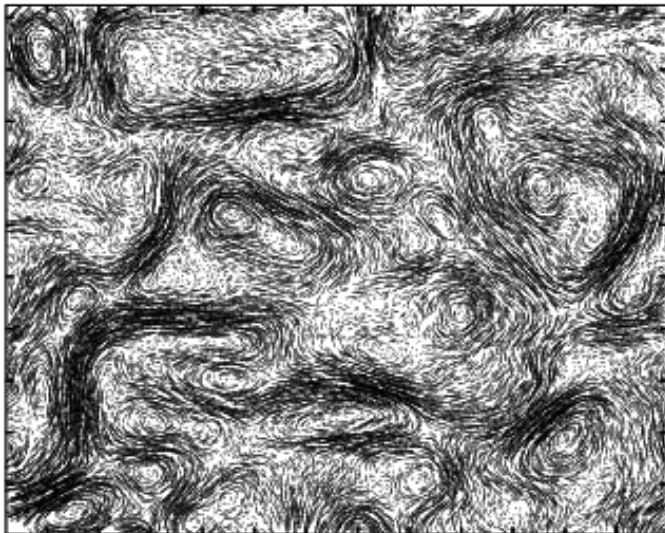


FIG. 2: Raw particle tracks obtained from the stratified layer over four consecutive frames (0.07 s).

forcing,  $\nu$  is the fluid kinematic viscosity, and Einstein summation is used throughout. The linear term with coefficient  $\alpha$  represents the effects of frictional drag owing to the container bottom. Although such a description is broadly consistent with a number of experimental results, the detailed correspondence of the electromagnetic layer flow with the linearly-damped 2D Navier-Stokes equation has not been performed [7, 13].

In the set of experiments presented here, the system described above is modified slightly by replacing the lower layer of fluid with Fluorinert FC-75 and the upper layer by a dense salt water solution of 20% by mass NaCl with a small amount of liquid detergent added to lower surface tension and help with dissolution of tracer particles. The Fluorinert has a density 1.8 times that of water with nearly the same viscosity, which allows for much stronger stratification than in the case of two salt-water solutions. It is also a strong dielectric so that only the upper salt-water layer is electromagnetically forced. Finally, and perhaps most importantly, the Fluorinert and water are immiscible. These combined features allow the Fluorinert system to maintain stratification indefinitely, allowing the salt water layer to be driven harder than in previous systems [21].

The experimental apparatus, shown schematically in Fig. 1, consists of a 0.3 cm thick layer of salt-solution suspended over a 0.3 cm thick layer of Fluorinert. The layers are contained in a 40 cm  $\times$  20 cm box with reservoirs at each end across which copper electrodes are placed in the fluid. An alternating square-wave current with frequency 0.5 Hz and amplitude 0.75 amps is driven through the salt solution. A set of 1.27 cm diameter rare-earth magnets of approximately 0.7 T residual field strength are arranged with alternating field direction in a 20 cm

$\times$  20 cm square array with a period of 2.54 cm and oriented at 45° with respect to the current direction. The combination of the current and the magnetic field produces a Kolmogorov-like forcing [7, 20] of alternating shear bands with the shear direction along  $\hat{y}$  and periodicity  $r_{inj} \approx 1.8$  cm in the  $\hat{x}$  direction, which implies  $k_{inj} \equiv 2\pi/r_{inj} = 3.5$  rad/cm. Using the layer depths of 0.3 cm yields  $\alpha \approx 0.125$  Hz for the frictional coupling assuming a simple linear shear in the Fluorinert. The salt solution upper layer has a viscosity around 1.15 that of water.

To obtain Eulerian velocity fields and particle trajectory information, the upper salt-solution layer was seeded with polycrystalline powder with mean diameter 75  $\mu\text{m}$  and density 0.98 gm/cc. Images of the particle fields, illuminated using several Xenon short-arc flash lamps, were obtained with a 1280  $\times$  1024 pixel CCD camera at a frame rate of 60 Hz. The velocity field was obtained from image pairs using particle tracking velocimetry derived from two earlier methods [22, 23]. From a typical pair of images, of order  $3 \times 10^4$  particle tracks were obtained and then interpolated to a 126  $\times$  100 velocity field array. A typical field of raw particle tracks is shown in Fig. 2.

From this raw data one can obtain particle trajectories in two ways: splice together raw particle tracks or use the interpolated Eulerian fields to generate particle trajectories by solving the advection equation. The later technique will be used here. The generated particle tracks solve the equation

$$\frac{d\mathbf{r}}{dt} = \mathbf{u}(\mathbf{r}(t), t), \quad (4)$$

where  $\mathbf{r}(t)$  is the position of the tracer particle at time  $t$ , bicubic interpolation is used to approximate  $\mathbf{u}$  at the

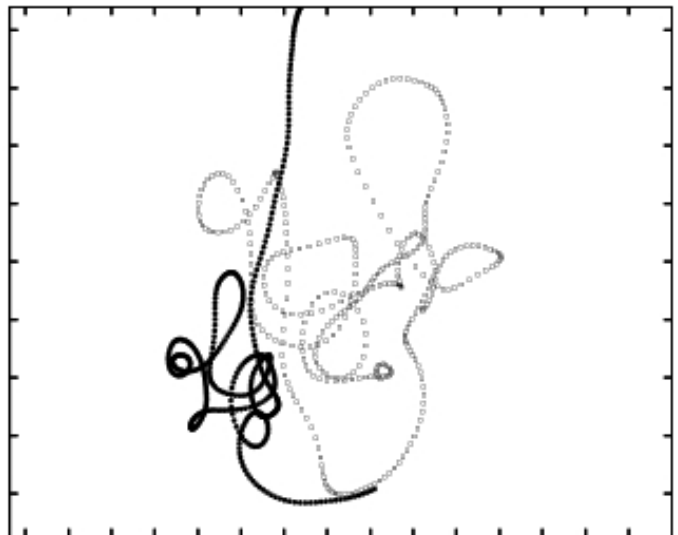


FIG. 3: Typical time-spliced real particle trajectory and a trajectory computed from dynamic velocity field data .

particle position, and fourth-order Runge Kutta is used to perform the time integration. Typical time-spliced particle trajectories and generated trajectories are shown in Fig. 3.

The turbulent state that we obtain for the stratified layer system described above can be characterized by several of its Eulerian ensemble-averaged statistics. The average energy per unit mass  $E = u_{rms}^2/2$  is  $8.4 \text{ cm}^2/\text{s}^2$  ( $u_{rms} = 4.1 \text{ cm/s}$ ) and the average enstrophy  $\Omega = \omega_{rms}^2/2$ , where the vorticity  $\omega \equiv \nabla \times \mathbf{u}$ , is  $51 \text{ s}^{-2}$  ( $w_{rms} = 10.1 \text{ s}^{-1}$ ).

## RESULTS AND DISCUSSION

Our system displays two different ranges corresponding to predominantly inverse-energy transfer [24] for scales larger than the injection scale and direct-enstrophy transfer for scales smaller than the injection scale. Because of the relatively limited range of scales available in the experiments, it is important to firmly establish the extent of the spatial and temporal scales for each transfer range. Empirically, this is best done utilizing spectra: we find that turbulent range transitions are sharper in Fourier space than in real space. The Eulerian and Lagrangian energy spectrum for data obtained from the electromagnetic cell are shown in Figs. 4a and b, respectively. For the Eulerian spectrum,  $E(k)$  is calculated for individual velocity fields using  $\tilde{u}_i(k)\tilde{u}_i^*(k)/2$  and averaged over velocity fields from the entire run. The Lagrangian spectrum,  $E(f)$ , is calculated from the Lagrangian velocity correlation  $\langle u_i(t)u_i(t+\tau) \rangle$  using the Wiener-Kinchin theorem.

We begin by identifying the length scales over which there is an inverse-energy range. According to previous results [13, 14, 19], this range occurs at wave numbers smaller than the injection wave number  $k_{inj} = 2\pi/r_{inj} = 3.5 \text{ rad/cm}$  and is characterized by a spectral scaling of  $E(k) \propto k^{-5/3}$ . To identify this range, we plot in the inset the local spectral exponent,

$$\chi_E \equiv \frac{d\{\log(E(k)/E(k_{inj}))\}}{d\{\log(k/k_{inj})\}}. \quad (5)$$

The value  $-5/3$  does not occur over any extended range. There is, however, a tight band of wave numbers smaller than  $k_{inj}$  over which the values of  $\chi_E$  are close to  $-5/3$ , namely  $1.65 \text{ cm}^{-1} < k < 2.64 \text{ cm}^{-1}$  (the dark bar in the inset plot). At wave numbers smaller than this range the spectral slope rises through zero and becomes positive corresponding to the large-scale saturation peak. wave numbers just in excess of this range are associated with the injection scales. We take this tight band as the inverse-energy range; the choice of this tight band as a “range” will be justified in later analysis. A best fit power law to the range yields a spectral exponent of  $-1.2$ . Taking the point at  $k = 2.64 \text{ cm}^{-1}$  and assuming

$E(k) = C_0^E \epsilon^{2/3} k^{-5/3}$ , where  $\epsilon$  is the scale-to-scale energy transport rate (roughly the large-scale dissipation  $\alpha u_{rms}^2$ ), yields a value for the Eulerian-Kolmogorov constant of  $C_0^E \approx 6$ , in agreement with earlier numerical and experimental work [13, 14].

The same procedure is used to establish the direct-enstrophy range at wave numbers greater than  $k_{inj}$ . The spectra in the direct-enstrophy range is expected to scale as  $E(k) \propto k^{-3}$  in the absence of frictional dissipation [19]. With frictional dissipation, as is the case in the electromagnetic cell, the scaling exponent is expected to become more negative [15]. For wave numbers  $4.5 \text{ cm}^{-1} < k < 13 \text{ cm}^{-1}$ , indicated by a light bar in the inset,  $\chi$  has an average value of  $-5.7$ . This range is taken to be the direct-enstrophy range. Note that the scaling exponent is extremely steep when compared to the dissipation free expectation of  $-3$ , indicative of a large amount of external dissipation. The upper-limit of the direct-enstrophy range  $k = 13 \text{ cm}^{-1}$  corresponds to a length scale of  $5 \text{ mm}$ , which is comparable to the fluid layer depth of  $3 \text{ mm}$  where one might expect 3D effects to become important.

Establishing the time scales of the inverse-energy and direct-enstrophy ranges in the Lagrangian frame is done in the same manner as for Eulerian statistics. The dimensional expectation for the energy range is that  $E(f) \propto f^{-2}$  for frequencies smaller than the energy injection frequency,  $f_{inj} = 1.66 \text{ Hz}$ , which is about the eddy rotation frequency of an injection scale vortex. As in the Eulerian spectra, the Lagrangian spectra do not achieve a range over which the spectral scaling, measured by the exponent  $\chi_L$  defined in the same way as  $\chi_E$  and shown in the inset, achieves a constant  $-2$  value. It also does not have as clearly defined a range as the Eulerian spectrum. The region marked by the dark bar corresponding to frequencies between  $0.66 \text{ Hz}$  and  $1.28 \text{ Hz}$ , characterized by a spectral slope increase from a  $-2$  value to about  $-1$ , should be the inverse-energy-range. Below this range the spectral exponent is less than  $1$  corresponding to large-scale saturation, and above is the abrupt spectral exponent change associated with  $f_{inj}$ . A best fit power law to this range yields an exponent of  $-1.6$ . Taking the point at  $f = 1.28 \text{ Hz}$  and assuming  $E(f) = C_0^L \epsilon f^{-2}$  yields a Lagrangian-Kolmogorov constant of  $C_0^L \approx 10$ . The enstrophy range, for which a simple dimensional prediction does not exist, is taken to be the range of frequencies spanning  $1.87 \text{ Hz}$  to  $4.27 \text{ Hz}$ , over which the spectral exponent is around  $-4.9$ . The frequency  $4.27 \text{ Hz}$  corresponds to a  $0.23 \text{ s}$  time scale, which is the same as the Lagrangian correlation time calculated by integration of the normalized two-point correlation. The steep spectral exponent is in agreement with earlier geophysical observations [25].

We now consider Eulerian and Lagrangian velocity statistics as measured by  $n^{\text{th}}$  order moments of velocity differences, i.e., structure functions,  $S^{(n)}(r)$  and  $D^{(n)}(\tau)$ ,

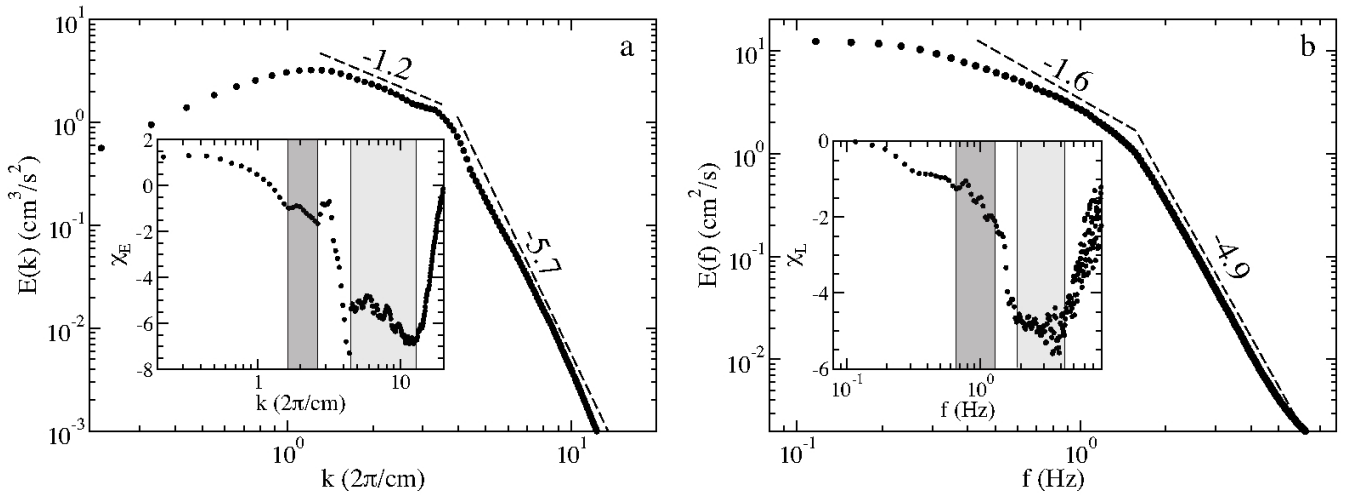


FIG. 4: (a) Eulerian and (b) Lagrangian energy spectra. Insets show the behavior of the respective spectra's local scaling exponent. The proposed ranges of wave numbers (Eulerian) and frequencies (Lagrangian) over which there is an inverse-energy range is denoted by a dark bar in the insets. The proposed direct-entropy range is likewise indicated by a light bar. Best fit power laws over the suggested ranges are displayed by lines with the scaling exponents given. See the text for the exact ranges and power laws.

respectively. Averages for the structure function calculation are taken over ensembles of realizations, and spatial and temporal homogeneity of signals is assumed so that the moments do not depend on absolute position  $\mathbf{x}$  or time  $t$ . For the inverse energy range of two-dimensional turbulence, we have dimensional predictions for scaling exponents:  $S^{(n)}(r) \propto (\epsilon r)^{n/3}$  and  $D^{(n)}(\tau) \propto (\epsilon \tau)^{n/2}$ . In the enstrophy range for Eulerian statistics, we expect  $S^{(n)}(r) \propto r^n$ , indicating a smooth velocity field for which the linear order term in the Taylor expansion is dominant. For Lagrangian statistics, at small time scales where acceleration is approximately constant, we expect  $D^{(n)}(\tau) \propto \tau^n$ . Thus, we expect scaling in the enstrophy range to have exponents between  $n$  and  $n/2$ .

We begin by looking at the second moments ( $n=2$ ) which are displayed in Fig. 5. Inset in these plots are the local exponents for the second moments, defined as

$$\xi_E^{(n)} \equiv \frac{d\{\log(S^{(n)}/u_{rms}^n)\}}{d\{\log(r/r_{inj})\}}, \quad (6)$$

$$\xi_L^{(n)} \equiv \frac{d\{\log(D^{(n)}/u_{rms}^n)\}}{d\{\log(\tau/\tau_{inj})\}}. \quad (7)$$

A scaling range where  $\xi$  has a constant value is not observed. This is unsurprising given the small extent of the ranges as identified by spectral analysis.

The second moments are frequently used in lieu of spectral analysis to identify scaling ranges. This is done because, in the limit of long scaling ranges, the results should yield similar ranges (the Wiener-Kinchen theorem links the spectra with the second-moments through the correlation function). For small ranges, however, simply assuming this correspondence is dangerous. If we deter-

mine temporal and spatial scales utilizing these moments by, for example, bracketing ranges with the expected scaling exponents, we get inconsistent results. In particular, we expect the Eulerian second moment to scale as  $r^{2/3}$  in the inverse energy range. Looking for the region where  $\xi_E^{(2)}$  assumes a value of 0.66 would yield a length scale of around 1.44 cm, which is significantly smaller than the injection scale of 1.8 cm, *i.e., in the enstrophy range of length scales*. A similar phenomenon happens for time scales of the Lagrangian second moment. The time scale at which  $\xi_L^{(2)}$  assumes the expected value of 1 is well within the spectrally identified enstrophy range.

Given the lack of correspondence between real and spectral space results, it is interesting to ask if ranges identified spectrally are reflected in their real space counterparts. It is also valid to consider why we use the spectral method for identifying ranges in the first place since it was an empirical decision to do so. In the rest of this paper, we demonstrate that although the spectral ranges are not easily identified in the direct moments, they correspond directly to features of the PDF shape, that is, when we investigate velocity statistics using ESS. For the moment, simply assuming the spectrally identified ranges are correct (marked by a dark and light bar again), we get best fit power laws to the second moments that significantly deviate from expected behavior, see Fig. 5.

The Eulerian and Lagrangian velocity-difference moments of order  $1 \leq n \leq 6$  are shown in Fig. 6, and the insets show the local exponents with dark and light bars to indicate the spectrally-identified scaling ranges. To fit exponents confidently to high-order moments, scaling is needed over an extensive range. Unsurprisingly, based on

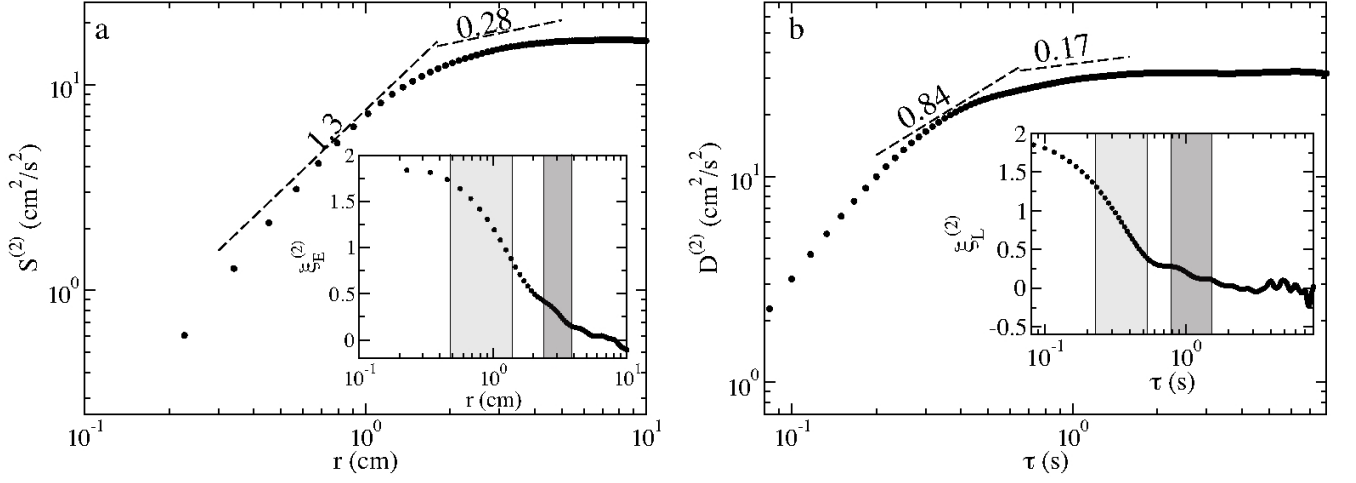


FIG. 5: (a) Eulerian and (b) Lagrangian second-order structure functions. Insets show the behavior of the respective structure function local scaling exponents. The ranges of length (Eulerian) and time (Lagrangian) for the inverse-energy regime, determined from spectra, are denoted by dark bars in the insets. The direct-enstrophy ranges, likewise determined from spectra, are indicated by light bars. Best fit power laws over the suggested ranges are displayed by lines with the scaling exponents given. See the text for the exact ranges and power laws.

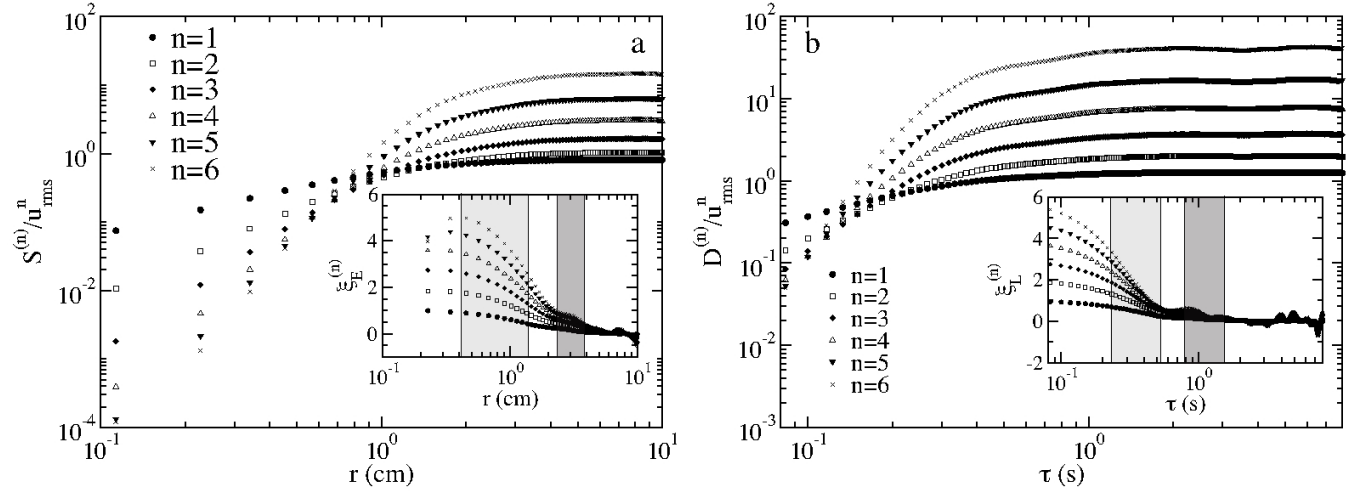


FIG. 6: (a) Eulerian and (b) Lagrangian  $n^{\text{th}}$ -order structure functions normalized by  $u_{rms}^n$ . Insets show the behavior of the respective structure function local scaling exponents. The ranges of length (Eulerian) and time (Lagrangian) for the inverse energy regime, determined from spectra, are denoted by dark bars in the insets. The enstrophy-ranges, likewise determined from spectra, are indicated by light bars.

the previous spectral analysis, no such ranges are visible at moments of any order. Although long ranges are not seen for either the Eulerian or Lagrangian data, the exponents of the moments behave in a very similar manner at different order, suggesting distinct changes in the behavior of the local exponents over the spectrally identified ranges. Because constant exponents are not observed in the measured range, we are forced to draw conclusions based on ESS analysis.

We normalize the local exponents by the second-order

local exponent and scale by the expected value of  $n/2$ , *i.e.*, we use ESS. By doing this normalization, we are looking at the change in PDF shape over a range of scales. This is shown in Fig. 7. There is very different behavior for the Lagrangian and Eulerian analysis. For self-similarity to hold over a range (that is, an unchanging PDF shape), the value of the normalized local exponent must be unity, for all  $n$ , over that range, *i.e.*, the higher moments are simply scaling as a power of the second moment. Given these observations, it is possible to draw

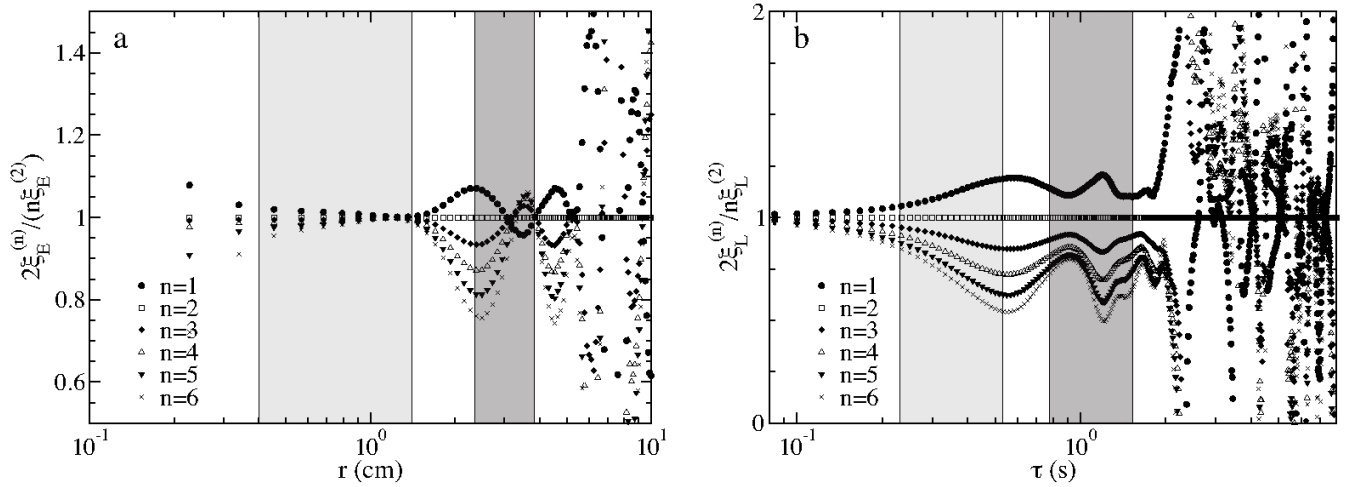


FIG. 7: The structure functions local exponent for orders  $1 \leq n \leq 6$  normalized by  $n\xi(2)/2$  for (a) the Eulerian frame and (b) the Lagrangian frame. The ranges of length (Eulerian) and time (Lagrangian) for the inverse energy regime, determined from spectra, are denoted by dark bars in the insets. The enstrophy-ranges, likewise determined from spectra, are indicated by light bars. A range with value of unity for *all* of the normalized local exponent indicates that the PDF shape is constant.

some stronger conclusions.

The spectrally-identified ranges, which seemed arbitrary and did not clearly correspond to any particular behavior in the real-space statistics, become more transparent. The enstrophy range in the Eulerian statistics is characterized by a near unity grouping of all the moments. At the upper-end of the Eulerian enstrophy range we see a sharp change in the behavior of the exponents where they begin to deviate from one. This deviation reaches a peak at the low-end of the inverse energy range and quickly collapses back to near unity. The conclusion we draw from this behavior is that, in our system, both the energy and enstrophy range Eulerian velocity difference statistics are tending to behave self-similarly (*i.e.*, normalized exponents tending to unity). This is in agreement with earlier observations of the unnormalized quantities. [13, 14, 15]. We speculate, given previous numerical work with more extensive ranges, that the small deviation from unity that we observe, in the limit of a long range well removed from injection effects, should settle down to unity. The average value of the exponent ratio for both the Eulerian energy and enstrophy ranges for a range of  $n$  is displayed in Fig. 8 as open symbols. A line marked K41 (for Kolmogorov 1941) indicates self-similar scaling.

The story is quite different for the Lagrangian results. The spectral ranges still find support, but in almost exactly the opposite manner: divergences from unity grow in the energy and enstrophy ranges while being reduced in the intermediate (injection) range (note that the vertical scales are different between Fig. 7a and b). Indeed, for the energy range, the maximal deviation from unity occurs in the center of the range, collapsing back to unity

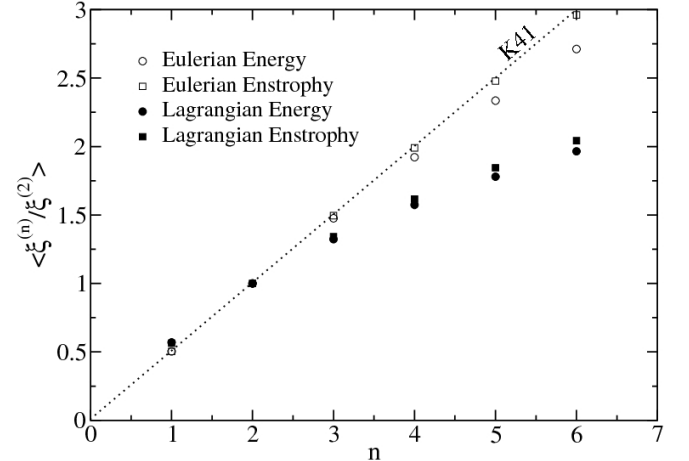


FIG. 8: The normalized local exponents for the velocity difference moments averaged over the inverse-energy and direct enstrophy ranges in both the Eulerian and Lagrangian frame. Strict self-similarity over a given range would be indicated by collapse of the moments on the K41 (Kolmogorov 1941) line.

only after the outer scale is reached. This allows us to speculate that, even in the limit of long ranges, the energy range will continue to deviate from unity and display a lack of similarity. Interpretation of what occurs in the enstrophy range is somewhat more complicated. There is a deviation from unity, but whether this is a residual result of a small range and the close proximity to the injection scale is uncertain. In the limit of a long range, the majority of the enstrophy range may approach unity. This would be unsurprising because the spectral



statistics indicate a very smooth enstrophy range in the Lagrangian frame. Therefore, we expect velocity difference statistics to be dominated by first-order terms in the series expansion as in the Eulerian case. Without further measurements it is difficult to extrapolate based on this data. As with the Eulerian data, the average local exponent over the energy and enstrophy ranges for a range of  $n$  is displayed in Fig. 8 as close symbols. Deviation from similarity is readily apparent when compared with the Eulerian statistics.

The data at very large scales and times are not well enough converged to draw any conclusions about statistical behavior past the outer scale. The dissipative ranges (small  $r$  and  $\tau$ ), however, are well converged and observably different. The Eulerian range is characterized by an increasingly non-self-similar dissipation range, whereas the Lagrangian frame quickly collapses to a state of similarity. For the Eulerian frame, this is most likely indicative of a spatially inhomogeneous viscous dissipation - a similar observation is found in three-dimensional turbulence [2]. For the Lagrangian frame, the collapse to similarity is surprising. It may be misleading, however. At these short times, linear order terms in a expansion are dominant, and therefore velocity difference may not be able to capture deviations from similarity well, much as is the case for the velocity difference statistics in the Eulerian enstrophy range.

## CONCLUSIONS

We have considered velocity difference statistics in two-dimensional turbulence for both the Eulerian and Lagrangian frames. Eulerian statistics are investigated and compared with earlier results, and novel Lagrangian statistics are presented. As in prior experiments, the extent of the inverse-energy range and direct-enstrophy range are limited. The limited range has two major effects: the scaling exponents are different in magnitude from the dimensional predictions, and there is no easily identifiable correspondence between ranges in spectra and behavior of moments. These observations are not unexpected for systems without extended scaling ranges.

Further analysis using ESS, however, yields a number of important insights. First, the results in the Eulerian frame are consistent with the broadly self-similar results found in prior experiments and simulations for velocity difference statistics, in spite of a lack of scaling. Second, the Lagrangian frame velocity difference statistics are not self-similar, a conclusion more strongly evident in the inverse-energy range than in the direct-enstrophy range. Finally, the dissipation ranges are not self-similar in the Eulerian frame, whereas they collapse to self-similar form for the Lagrangian frame.

In addition to our main conclusions, we can provide two further insights from an analysis perspective. First is

that careful identification of spectral ranges are echoed in the behavior of the moments local exponent ratios fairly precisely. This was somewhat surprising since it has been believed that moment ranges do not necessarily line up in detail with spectral ranges, in particular when those ranges are small. The data here indicate otherwise. Second, the local exponent ratio is effectively a derivative quantity. It measures the relative change in the behavior of the PDF's shape over a range of scales. Even when the moment ranges are small, the shape of the corresponding PDF changes rapidly.

## ACKNOWLEDGMENTS

This work was performed for the U.S. Department of Energy under Contract # DE-AC52-06NA25396. The authors benefited from conversations with Colm Connaughton and Mahesh Bandi.

- 
- [1] G. K. Batchelor, *The theory of homogenous turbulence* (Cambridge University Press, 1982, c1953).
  - [2] U. Frisch, *Turbulence: the legacy of A.N. Kolmogorov* (Cambridge University Press, 1995).
  - [3] A. S. Monin and A. M. Yaglom, *Statistical fluid mechanics; mechanics of turbulence* (MIT Press, 1975, c1971).
  - [4] S. B. Pope, *Turbulent flows* (Cambridge University Press, c2000).
  - [5] G. Falkovich, K. Gawedzki, and M. Vergassola, *Reviews of Modern Physics* **73**, 913 (2001).
  - [6] M. Jullien, J. Paret, and P. Tabeling, *Physical Review Letters* **82**, 2872 (1999).
  - [7] M. K. Rivera and R. E. Ecke, *Physical Review Letters* **95**, 194503 (2005).
  - [8] S. Ott and J. Mann, *Journal of Fluid Mechanics* **422**, 207 (2000).
  - [9] H. Xu, M. Bourgoïn, N. Ouellette, and E. Bodenschatz, *Physical Review Letters* **96**, 024503 (2006).
  - [10] K. Sreenivasan and B. Dhruva, *Progress of Theoretical Physics Supplement* pp. 103–20 (1998).
  - [11] L. Biferale, G. Boffetta, A. Celani, B. J. Devenish, A. Lanotte, and F. Toschi, *Physical Review Letters* **93**, 064502 (2004).
  - [12] R. H. Kraichnan, *Physics of Fluids* **13**, 22 (1970).
  - [13] J. Paret and P. Tabeling, *Physics of Fluids* **10**, 3126 (1998).
  - [14] G. Boffetta, A. Celani, and M. Vergassola, *Physical Review E* **61**, R29 (2000).
  - [15] Y. K. Tsang, E. Ott, T. M. A. Jr., and P. N. Guzdar, *Physical Review E* **71**, 066313 (2005).
  - [16] G. Eyink, *Physical Review Letters* **74**, 3800 (1995).
  - [17] L. Biferale, M. Cencini, A. Lanotte, D. Vergni, and A. Vulpiani, *Physical Review Letters* **87**, 124501/1 (2001).
  - [18] R. Benzi, S. Ciliberto, R. Tripiccone, C. Baudet, F. Massaioli, and S. Succi, *Physical Review Letters* **48**, R29 (1993).



- [19] R. Kraichnan and D. Montgomery, Reports on Progress in Physics **43**, 547 (1980).
- [20] N. Bondarenko, M. Gak, and F. Dolzhansky, Izvestiya Akademii Nauk SSSR Fizika Atmosfery I Okeana **15**, 1017 (1979).
- [21] J. Paret and P. Tabeling, Physical Review Letters **79**, 4162 (1997).
- [22] M. Ishikawa, Y. Murai, and F. Yamamoto, Measurement Science Technology **11**, 677 (2000).
- [23] K. Ohmi and H. Li, Measurement Science & Technology **11**, 603 (2000).
- [24] S. Chen, R. Ecke, G. Eyink, M. Rivera, M. Wan, and Z. Xiao, Physical Review Letters **96**, 1 (2006).
- [25] V. Rupolo, B. Hua, A. Provenzale, and V. Artale, Journal of Physical Oceanography **26**, 1591 (1996).